

# Journal of Materials Chemistry B

Accepted Manuscript



This is an *Accepted Manuscript*, which has been through the Royal Society of Chemistry peer review process and has been accepted for publication.

*Accepted Manuscripts* are published online shortly after acceptance, before technical editing, formatting and proof reading. Using this free service, authors can make their results available to the community, in citable form, before we publish the edited article. We will replace this *Accepted Manuscript* with the edited and formatted *Advance Article* as soon as it is available.

You can find more information about *Accepted Manuscripts* in the [Information for Authors](#).

Please note that technical editing may introduce minor changes to the text and/or graphics, which may alter content. The journal's standard [Terms & Conditions](#) and the [Ethical guidelines](#) still apply. In no event shall the Royal Society of Chemistry be held responsible for any errors or omissions in this *Accepted Manuscript* or any consequences arising from the use of any information it contains.



## ARTICLE

## Design and Application of a Smart Nanodevice by Combining Cationic Drug Delivery and Hyperthermia for Cancer Apoptosis

Arathyram Ramachandra Kurup Sasikala<sup>1</sup>, Afeesh Rajan Unnithan<sup>1,2\*</sup>, Chan Hee Park<sup>1,2\*</sup>, Cheol Sang Kim<sup>1,2\*</sup>

Received 00th January 20xx,  
Accepted 00th January 20xx

DOI: 10.1039/x0xx00000x

www.rsc.org/

Multifunctional magnetic nanoparticles have been gained ample attention in the field of nanomedicine in recent years. Here, a novel superparamagnetic core-shell manganese ferrite nanoparticles (MFNP)-encapsulated mesoporous silica nanoparticles (MSMFNPs) loaded with anticancer drug doxorubicin (DOX) for the combined application of hyperthermia and chemotherapy were developed and tested in vitro. Our results indicate that DOX-MSMFNPs achieved a favorable hyperthermic response in an alternating magnetic field in addition to cancer cell-specific cationic DOX release due to the cleavage of amide bonds at acidic pH and synergistically contributed towards an enhanced tumoricidal effect.

### 1. Introduction

In recent years, multifunctional magnetic nanoparticles (MFMNPs) have gained ample attention in the field of nanomedicine.<sup>1-3</sup> The potential biomedical applications of MFMNPs include as a magnetic resonance contrast agent in magnetic resonance imaging (MRI)<sup>4</sup>, magnetic hyperthermia for cancer treatment<sup>5</sup>, magnetic force-assisted drug delivery<sup>6</sup>, cell and tissue targeting, stimuli-responsive drug delivery<sup>7, 8</sup>, and biosensing.<sup>9</sup> The multifunctionality of magnetic nanoparticles (MNPs) has been achieved through various surface functionalization strategies.<sup>10, 11</sup> Silica has gained widespread interest as an inorganic surface functionalization agent for MNPs. Silica has excellent colloidal stability, and has enormous potential for further functionalization through the binding of various biological ligands. These factors make silica an ideal nanosystem for clinical nanomedicine.<sup>12, 13</sup>

There are high expectations for the potential of cancer therapy based on a combination of hyperthermia and chemotherapy in a single platform.<sup>14, 15</sup> The potency and selectivity of drugs for anticancer treatment have improved over the past decades, mainly because of the introduction of a plethora of drug delivery systems that combine a nanoplatform with both existing and newly designed drugs.<sup>16</sup> Among them, mesoporous silica nanoparticles (MSNPs) are receiving increased attention. MSNPs can house sizable amounts of cargo in their mesopores, and capping the pore entrances with different nanogates permits stimuli-responsive drug delivery.<sup>17</sup> Therefore by incorporating MNPs on MSNPs, we can better achieve the promising role of combination therapies for the improved anticancer efficacy.<sup>18</sup>

<sup>1</sup>Department of Bionanosystem Engineering, Graduate School, Chonbuk National University, Jeonju 561-756, Republic of Korea.

<sup>2</sup>Mechanical Design Engineering, Chonbuk National University, Jeonju 561-756, Republic of Korea.

A multitude of magnetic materials with exploitable heating efficiency are currently under intense investigation for various biomedical applications including hyperthermia.<sup>19</sup> The major challenges emerged in preparing MNP for hyperthermia include the development of novel MNPs with high heating ability (measured by specific absorption rate (SAR)) and temperature control of magnetic nanoparticles for in vivo application.<sup>20</sup> Therefore in pursuit of novel heat mediators, ferrite nanoparticles have emerged as a promising candidate due to their facile fabrication, chemical stability and intrinsic biocompatibility along with unique heat generation property.<sup>21</sup> Among magnetic ferrite nanoparticles, manganese ferrite nanoparticles (MFNPs) have generated interest due to high levels of biocompatibility and heat generation.<sup>22</sup> In particular, MFNPs possesses a low Curie point ( $T_c = 573$  K), and the  $T_c$  can be adjusted to the therapeutic temperature to act as a smart platform for self-controlled hyperthermia treatment.<sup>23</sup>

In this study, we report the fabrication of novel, superparamagnetic core-shell MFNP-encapsulated mesoporous silica nanoparticles (MSMFNPs) loaded with the anticancer drug doxorubicin (DOX) for the combined application of hyperthermia and chemotherapy for synergistic anticancer treatment. Preparation of monodisperse mesoporous MNPs was carried out by thermal decomposition followed by hydrolysis of Tetraethyl orthosilicate (TEOS) in a water-in-oil microemulsion. MFNPs were used as seeds, with the subsequent addition of N-(2-aminoethyl)-3-aminopropyltrimethoxysilane (AEAP3). Till date many studies were reported with mesoporous silica magnetic nanoparticles for drug delivery application. But in our study the nanoparticles were further functionalized with 1, 2-cyclohexanedicarboxylic anhydride (CDA) as a click linker, to couple DOX to the porous silica shells via amide linkage. The coupled DOX molecules are relatively stable at a neutral pH (~7.4), but can be disassembled with a decrease in pH. The DOX molecules show an obvious release at a low pH (5.0–6.0) due to the hydrolysis of the amide bonds. This release property accounts for the efficacy of cationic drug delivery corresponding to a tumor environment. Thus, the DOX loaded MSMFNPs can act as a multifunctional nanopatform for synergistic anticancer treatment. They act as both a hyperthermic agent that delivers heat when an alternating magnetic field (AMF) is applied, as well as a chemotherapeutic agent that provides pH-dependent DOX release in a cancerous environment.

## 2. Experimental Section

**Materials:** Iron (III) acetylacetonate [ $\text{Fe}(\text{acac})_3$ ], Manganese (II) acetylacetonate [ $\text{Mn}(\text{acac})_2$ ], oleic acid, oleylamine (70%), benzyl ether (98%), hexane(99.9%), ethanol, 1-hexanol anhydrous (99%), ammonia solution ( $\text{NH}_4\text{OH}$ ; 28-30 wt % in water), Triton X-100, cyclohexane (99.5%), N-(2-aminoethyl)-3-aminopropyltrimethoxysilane (AEAP3), dimethyl sulfoxide (DMSO; 99%), 1,2-cis-cyclohexanedicarboxylic anhydride (98%), triethylamine (98%), tetraethoxysilane (TEOS; 99.999%),

and doxorubicin hydrochloride (98%) were purchased from Sigma Aldrich, South Korea.

**Synthesis of manganese ferrite nanoparticles (MFNPs):** Superparamagnetic monodisperse MFNPs were synthesized via high-temperature reduction/decomposition reaction using metal acetylacetonate.<sup>21</sup> Typically, a one-pot reaction was carried out with metal precursors  $\text{Fe}(\text{acac})_3$  (10 mmol),  $\text{Mn}(\text{acac})_2$  (5mmol), surfactants [oleic acid (6 mmol) and oleylamine (6 mmol)], and solvent [benzyl ether (35 ml)] heated to  $165^\circ\text{C}$  under nitrogen gas flow protection for 30 min. Subsequently, the mixture was heated to  $280^\circ\text{C}$  and maintained at this temperature for 30 min. The black-colored mixture (MFNPs) was allowed to cool, precipitated by the addition of ethanol, isolated using centrifugation, and followed by subsequent re-dispersion into hexane. The previous washing procedure was repeated at least three times, and the MNPs were stored in a sealed glass vial at  $4^\circ\text{C}$  by dispersion into hexane.

**Synthesis of mesoporous core-shell-MF-silica nanoparticles (MSMFNPs):** The MSMFNPs were fabricated by hydrolyzing TEOS in a water-in-oil microemulsion with MFNPs as seeds.<sup>24</sup> MFNPs were dispersed in cyclohexane (1 mg/mL), and 0.5 ml of the dispersion was injected into a mixture of 1.77 g of Triton X-100, 1.6 ml of anhydrous 1-hexanol and 7 ml of cyclohexane under a strong vortex for about 1 h. Then, 0.5 ml of ammonia solution (28–30% ammonia solution: water 1:4) was added to the above solution and shaken for 1 h. Finally, 25 mL of TEOS was added, and the mixture was allowed to react for 24 h. In order to prepare the porous silica nanoparticles, 25 ml of AEAP3 were injected into the above reaction mixture for another 24 h. The product was precipitated by adding excess anhydrous ethanol, and separated by centrifugation (9000 rpm). This process was repeated at least three times to completely remove the unreacted TEOS. The precipitate was then washed three times with deionized water. The resulting product was stored in deionized water for further usage.

**Synthesis of DOX-loaded mesoporous core-shell-MF-silica nanoparticles (DOX-MSMFNPs):** In order to prepare the pH-sensitive smart DOX-MSMFNPs for cancer-specific drug release, further modification of MSMFNPs was carried out using 1,2-cyclohexanedicarboxylic anhydride (CDA). A total of 40 mg of MSMFNPs were dispersed in DMSO and sonicated for 10 min. 1,2-cis-Cyclohexanedicarboxylic anhydride (10 mmol) was added to the above mixture, and magnetically stirred for 2 h. The grafted nanoparticles were separated by centrifugation at 9000 rpm and mildly washed three times with DMSO. Varying amounts (2, 4, 6, 8 and 10 mg/ml concentrations) of CDA grafted MSMFNPs were then prepared from the stock (40 mg in 10 ml: all loading was done in triplicate), with serial dilutions using DMSO and sonicated for 2 min. A fixed amount of DOX (1 mg/ml in DMSO) was added to each suspension of grafted MSMFNPs, and  $50\mu\text{L}$  of triethylamine was subsequently added to each suspension. The resulting dispersion was maintained at room temperature for 24 h with constant mechanical stirring. The drug loaded MSMFNPs (DOX-MSMFNPs) were separated from the free drug molecules by centrifugation, and mildly washed three times with pH 7.4

phosphoric acid buffer solution. The resulting DOX-MSMFNPs were stored at 4°C. The concentration of DOX in the supernatant was measured using the UV spectra of DOX, using a previously-obtained calibration curve with dilution series. The amount of drug incorporated into the DOX-MSMFNPs was estimated using the equation:<sup>25</sup>

$$\% \text{ Entrapment efficiency} = \frac{\text{Initial concentration of drug} - \text{Drug content in the supernatant}}{\text{Initial concentration of drug}} \times 100$$

For comparison, we also measured the entrapment efficiency of DOX molecules in the MSMFNPs without the aid of click linker (CDA). The same procedure was carried out to load the drug in MSMFNPs without CDA click linker.

**Characterization of techniques:** X-ray powder diffraction analysis was carried out on a Rigaku X-ray diffractometer (Cu K $\alpha$ ,  $k = 1.54059 \text{ \AA}$ ) over Bragg angles ranging from 20 to 80°. The size, morphology and crystallography of the synthesized MFNPs and MSMFNPs were investigated via transmission electron microscopy (TEM, JEOL JEM, Japan), and the corresponding specific area electron diffraction (SAED) patterns were also examined. The bonding configurations of the samples were characterized by means of their FTIR spectra using a Paragon 1000 Spectrometer (Perkin Elmer). The surface charge was characterized by using a zeta potential and particle size analyzer (ELS-8000; Photal Otsuka Electronics Co, Ltd, Osaka, Japan). The magnetic characterization was carried out on a physical property measurement system (PPMS, model 6000). DOX binding and release characteristics were analyzed by capturing the UV-visible absorption spectra (HP 8453 UV-vis spectroscopy system, Germany) at a wavelength of 490 nm. The cells were observed under a LSM510 confocal laser-scanning microscope (Carl Zeiss, Germany).

**In vitro hyperthermia studies and SAR measurements:** Alternating magnetic field (AMF)-induced heating ability of MSMFNPs was studied using an alternating magnetic field generator (OSH-120-B, OSUNG HITECH, Republic of Korea). Typically, aqueous solutions of MSMFNPs at various concentrations (6, 8, 10 mg/ml) were placed on the center of the water-cooled induction coil connected to the AMF generator. The strength and frequency of the magnetic field were adjusted to 12.57 kA/m and 293 kHz, respectively. The samples were heated to 1200 s, and the heating characteristics were automatically recorded using a type-T thermocouples and real-time data acquisition system (NI-DAQ, National Instruments, USA) with LabVIEW software. Before each experiment, the temperature was calibrated and stabilized for 10 min. The heating efficiency of the samples was quantified by calculating the specific absorption rate (SAR), following the procedure that has been described previously.<sup>26</sup> The SAR values were calculated using the equation:

$$SAR = C \left( \frac{\Delta T}{\Delta t} \right) \frac{1}{m_{\text{magn}}}$$

where C is the sample-specific heat capacity calculated as the mass-weighted mean value of magnetite and water. The heat

capacity of MSMFNPs is not considered in the current study, since it is present at a low concentration. Thus, the heat capacity for water ( $4.186 \text{ J g}^{-1} \text{ K}^{-1}$ ) is only considered as the heat capacity of the sample.<sup>27</sup>  $\Delta T/\Delta t$  is the initial slope of the time-dependent temperature curve. The slope was initially obtained for 60 s once after the magnetic field was generated, as the curve was linear in this regime. The value of  $m_{\text{magn}}$  is considered the amount of magnetite per total amount of magnetite and water.

**Kinetics of pH-dependent drug release:** pH-dependent DOX release was analysed by performing a procedure often used to measure drug entrapment efficiency<sup>24</sup>. Typically, a predetermined concentration of drug-loaded nanoparticles (both CDA grafted DOX-MSMFNPs and CDA ungrafted DOX-MSMFNPs) was suspended in PBS buffer at varying pH levels, including physiological (pH=7.4) and acidic (pH=5). These samples were then placed in a shaking incubator at 37 °C. At different time intervals, 1 ml of release solution (PBS) was removed and replaced with 1 ml of fresh PBS in order to maintain a constant volume. The amount of DOX released was quantified by capturing the UV-visible absorption spectra (HP 8453 UV-vis spectroscopy system, Germany) at a wavelength of 490 nm. Triplicate samples were used to ensure accuracy.

**In vitro cell culture studies:** Murine fibroblast (NIH3T3) and mouse mammary carcinoma (4T1) cell lines were purchased from ATCC® (Manassas, VA, USA).

**Intracellular localization of MSMFNPs by 4T1 cell lines:** Intracellular localization studies were qualitatively performed using Prussian blue staining, to directly estimate the uptake of MSMFNPs. 4T1 cell lines were incubated with MSMFNPs with AMF (12.57 kA/m, 293 kHz) and without AMF for 5 min prior to incubation with 4T1 cells. Typically, 4T1 cells ( $5 \times 10^5$  cells/well) were seeded into an 8-well chamber slide (Lab-Tek2, Utah, USA) supplemented with medium (Thermo Scientific, Utah, USA). Both cell media contained 10% FBS and 1% penicillin-streptomycin, and cells were housed overnight at 37 °C in a humidified 5% CO<sub>2</sub> atmosphere. After 24 h, cells were washed twice with PBS to remove the medium. 1mg/ml of MSMFNPs was added to the cells in duplicate, a magnetic field was applied to one set field for 5 min, and both samples were incubated for another 2 hours to analyze intracellular uptake. Cells were fixed with 4% PFA for 15 min, 100  $\mu$ l of 4% potassium ferrocyanide (II) trihydrate and 4% HCl solution (in PBS) were added to each well, and cells were incubated for an additional 20 minutes. The cells were counterstained with a nuclear fast red stain. Cells stained blue indicate MSMFNP uptake. Images were collected using an inverted light optical microscope.

**In vitro biocompatibility of MSMFNPs:** The biocompatibility of MSMFNPs was evaluated against NIH3T3 cells lines using an MTS assay. The cells were seeded into a 96-well plate at a density of  $10^4$  cells/well. Cells were cultured for one day in an incubator with a humidified CO<sub>2</sub> atmosphere at 37 °C. In order to analyze cytocompatibility, varying concentrations of MSMFNPs (ranging from 2 mg/ml to 15 mg/ml) were added to the cells in triplicate and incubated for 24 hours. Twenty microliters of MTS reagent were added to each of the treated

wells, which were then incubated for 4 hours. Finally, the absorbance at 490 nm was measured using a microplate reader.

**In vitro anticancer studies:** The anticancer effects were tested on 4T1 cell lines in three scenarios, including hyperthermia alone (MSMFNPs-MH), drug alone (DOX-MSMFNPs) and combined hyperthermia and chemotherapy (DOX-MSMFNPs-MH). Cell viabilities were tested at different time intervals (12 h and 24 h) post-MH using an MTS assay. 4T1 cancer cells were seeded on 24-well plates at a density of  $5 \times 10^4$  cells/plate, and were cultured in DMEM medium in an incubator with a humidified 5% CO<sub>2</sub> atmosphere at 37°C. After a 24-h incubation period, the MSMFNPs-MH group was treated with 8 mg/ml of MSMFNPs, the DOX-MSMFNPs group was treated with 8 mg/ml of DOX-MSMFNPs, the DOX-MSMFNPs-MH group was treated with 8 mg/ml of DOX-MSMFNPs, and the samples were incubated for 2 more hours with an additional set of blank cells used as controls. All samples were taken in triplicate. The MSMFNPs-MH and DOX-MSMFNPs-MH groups were provided a hyperthermia treatment for 20 min (12.57 kA/m, 293 kHz) in a sterile environment. The DOX-MSMFNP group and control group were isolated into mini petri-dishes for the same amount of time to remove environmental effect on cell death. After hyperthermia treatment, fresh RPMI media was added, and cells were incubated in a 24-well plate for 30 minutes in a humidified 5% CO<sub>2</sub> environment at 37 °C. After 12 h, 50 µl of MTS reagent (Promega, USA) were added to each of the wells, and the plate was incubated for an additional 4 hours. The absorbance at 490 nm was then measured using a microplate reader. The same experiment was repeated, and the MTS assay was carried out after a 24 h incubation period. The proportions of live and dead cells in the DOX-MSMFNPs-MH group (after 12-h and 24-h incubation periods) were assessed by live/dead assay. The treated cells were stained with calcein AM (2 µM) and ethidium homodimer-1 (4 µM) for 30 min. Untreated cells were used as a control. The cell death mechanism of the DOX-MSMFNPs-MH group was analyzed using a Magic Red caspase detection kit. The apoptotic trend of the DOX-MSMFNPs-MH group after incubation periods of 12 and 24 h were compared with the control group. Nuclei were also stained with DAPI (4,6-diamidino-2-phenylindole, dilactate, Invitrogen, USA, 405 nm, blue) for 10 min. After magnetic hyperthermia application, cytoskeletal damage was assessed using the cytoskeletal F-actin stains Phalloidin (Alexa Fluor 488 Phalloidin, Molecular probes, USA, 488 nm, green) and Rhodamine B (Molecular probes, USA, 561 nm, Red) for the DOX-MSMFNPs-MH group (after 12 and 24 h incubation periods).

### 3. Results and Discussion

The size and morphology of synthesized MFNPs and MSMFNPs were investigated by transmission electron microscopy (TEM) (Figure 1). MFNPs possessed uniform distribution with spherical morphology (Figure 1A). The size distribution of MFNPs was less than 15 nm, and the crystalline phases of the MFNPs were clearly reflected in the selected-area electron

diffraction (SAED) patterns visualized using TEM (inset of Figure 1A). Energy dispersive x-ray spectroscopy (EDS) analysis of the MFNPs verified the presence of manganese in the MNPs (Figure 1B). TEM images of MSMFNPs (Figure 1C&D) demonstrate that MFNPs are completely encapsulated in the silica shell with a high degree of uniformity of the core/shell structure, in addition to having good monodispersibility in water. Higher magnification images of MSMFNPs (Figure 1D) depict that the cores of the nanoparticles are located in the centers of the silica shells, with a mean shell thickness of ~20 nm.

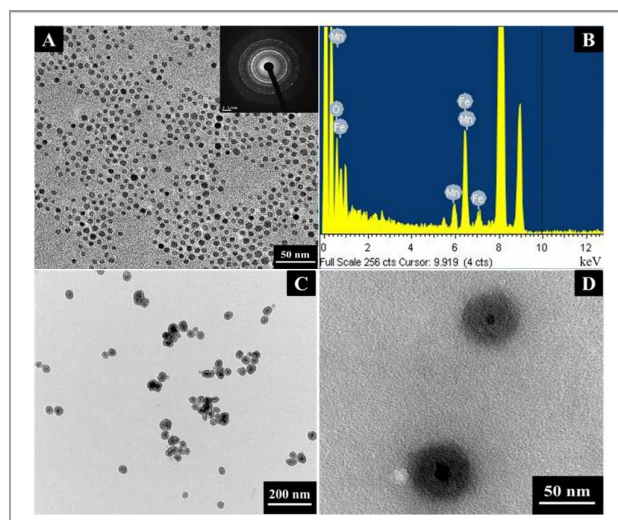


**Figure 1.** A) TEM images of MFNPs, B) EDS spectrum of MFNPs, C&D) TEM images of MSMFNPs.

The crystal structure of MFNPs and MSMFNPs was analyzed using powder X-ray diffraction (XRD) patterns (Figure 2A). The peak positions and the relative intensities of MFNPs and MSMFNPs were displayed. As shown in Figure 2A, all present peaks, such as (220), (311), (400), (422), (333) and (440), were indexed, as the cubic spinel ferrite structure of MnFe<sub>2</sub>O<sub>4</sub> (Jacobsite; JCPDS no. 74-2403) was confirmed in both MFNPs and MSMFNPs. A typical broad peak in MSMFNPs around 20° corresponded to the silica shell, confirmed the formation of MFNP encapsulated porous silica nanoparticles.<sup>28</sup>

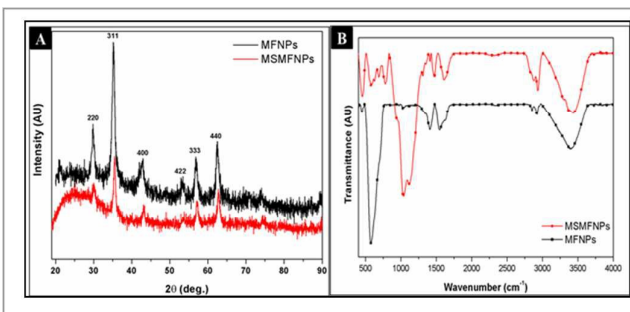


**Figure 2.** A) XRD patterns of MFNPs, B) FTIR spectra of MFNPs, C&D) TEM images of MSMFNPs.

The FTIR spectrum of MFNPs and MSMFNPs (Figure 2B) clearly exhibits the characteristic peak at 580 cm<sup>-1</sup> due to the vibrations of the Fe–O group from the MFNP.<sup>29</sup> Furthermore

the FTIR spectrum of MSMFNPs clearly indicate the characteristic peaks of silica at  $1040\text{ cm}^{-1}$  (asymmetric stretching  $\equiv\text{Si}-\text{O}-\text{Si}\equiv$ ) and  $935\text{ cm}^{-1}$  (symmetric stretching  $\equiv\text{Si}-\text{O}-\text{Si}\equiv$ ), confirming the formation of MFNP-porous silica nanoparticles.<sup>24</sup> The broad peak at  $\sim 3360\text{ cm}^{-1}$  is due to an overlap of hydrogen-bonded O–H and N–H stretching. The peaks at  $\sim 2930\text{ cm}^{-1}$  are due to stretching vibration of  $-\text{CH}_2-$  bonds. The multiple peaks between  $\sim 1320\text{ cm}^{-1}$  and  $1620\text{ cm}^{-1}$  are a consequence of the vibrations of amine groups.<sup>28</sup> Thus, FTIR analysis confirmed that the silica shells of MSMFNPs are functionalized in situ by hydroxyls, primary and secondary amine groups. The magnetic properties of MFNPs and MSMFNPs were investigated and found that both nanoparticles exhibit superparamagnetic behavior with no coercivity or remanence. (Figure S1 of the Supporting Information). Normally magnetic nanoparticles are widely used for targeted drug delivery applications. This is due to the magnetic property of the particles that can be controlled by an external magnet. Active targeting can be achieved by functionalizing the nanoparticles by targeting ligands such as folic acid receptor. In the present study, magnetic targeting can be easily employed due to the excellent magnetic property possessed by the MSMFNPs. The magnetic field-dependent heating ability of MSMFNPs was also measured at various concentrations (Figure 3B) to figure out the hyperthermic response and found that 8 mg/ml of MSMFNPs exhibited a hyperthermic temperature of  $\sim 42\text{ }^\circ\text{C}$  upon applying an AMF in 1200 sec with a comparable SAR value (Figure S2 of the Supporting Information).

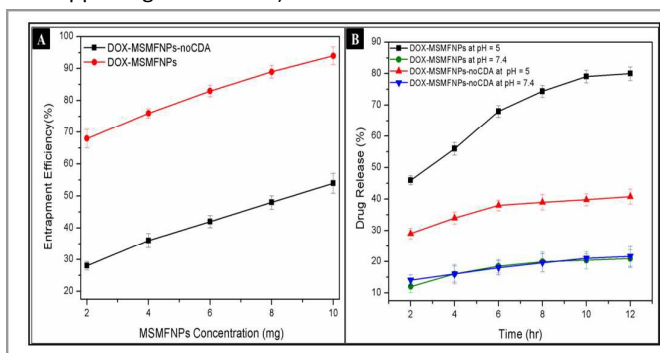


**Figure 3.** A) DOX entrapment efficiency, B) pH-dependent DOX release profiles

In order to exploit the MSMFNPs for the potential application of cationic drug delivery, the nanoparticles were modified with a click linker, 1, 2-cyclohexanedicarboxylic anhydride. CDA possesses an abundance of carboxyl and hydroxyl groups, and exhibits pH-sensitivity. Thus the CDA functionalized MSMFNPs with negative charges can bind oppositely charged DOX molecules through electrostatic interactions and hydrogen bonds,<sup>30</sup> ultimately forming a smart magnetic nanoplatform for pH-responsive anticancer drug release and hyperthermia through DOX-MSMFNPs.<sup>30</sup> The zeta potential values shown in supporting information figure S4 also confirms the binding of DOX to CDA functionalized MSMFNPs. Figure 3A shows the entrapment of DOX molecules at different concentrations of MSMFNPs. The results were compared with DOX-encapsulated

MSMFNPs without the aid of CDA linker. DOX encapsulation efficiency of both classes of MSMFNPs was observed to increase with the concentration of nanoparticles. The maximum entrapment efficiency exhibited by MSMFNPs (with CDA click linker) was  $\sim 94\%$  for 10 mg, whereas MSMFNPs without CDA exhibited an entrapment efficiency of only  $\sim 54\%$  for the same amount of nanoparticles. This indicates that in MSMFNPs without CDA, the DOX molecules are only loaded by physical adsorption rather than chemical bonding, as the hydroxyl groups of the MSMFNPs without CDA are unable to react with the amine group of the DOX molecules.<sup>28</sup> The high entrapment efficiency exhibited by CDA-modified MSMFNPs can be attributed to the abundance of carboxyl groups and hydroxyl groups that can effectively load drugs via electrostatic interactions and hydrogen bonding, along with the porous structure of the MSMFNPs.<sup>31</sup>

To establish pH-responsive DOX release kinetics, the release behaviours were studied at  $37\text{ }^\circ\text{C}$  in PBS buffers at different pH levels to mimic the tumor environment ( $\text{pH}=5.0$ ) and normal tissue or blood ( $\text{pH}=7.4$ ). As illustrated in Figure 3B, the release of DOX from both CDA-functionalized DOX-MSMFNPs and DOX-MSMFNPs not functionalized with CDA was pH-dependent. During a 12-h period,  $\sim 21\%$  of the DOX was released from the CDA-functionalized DOX-MSMFNPs that were maintained at a pH of 7.4, while  $\sim 80\%$  of the DOX was released at a pH of 5. These results clearly indicate the pH-dependent drug release. This can be explained by the pH-dependent coupling and hydrolysis of the amide bonds in CDA-functionalized DOX-MSMFNPs. At neutral pH, the amides are stable and negatively charged due to the carboxylic acid groups. Therefore, a small number of DOX molecules can be released, due to the strength of the amide bonds. Conversely, at low pH (5), the amides hydrolyze to regenerate the amine groups, resulting in a higher concentration of DOX.<sup>32</sup> For comparison, the pH dependent DOX release kinetics for DOX-MSMFNPs not functionalized with CDA was also analyzed (Figure 4B) and found that at low pH,  $\sim 41\%$  of DOX was released. This can be explained by the decrease in the strength of interaction between DOX and silica at low pH, due to the protonation of surface silanols.<sup>33</sup> Therefore the results clearly indicate the efficiency of CDA modified DOX-MSMFNPs for the enhanced DOX entrapment and improved cationic DOX release in a tumor environment in comparison to CDA unmodified DOX-MSMFNPs.

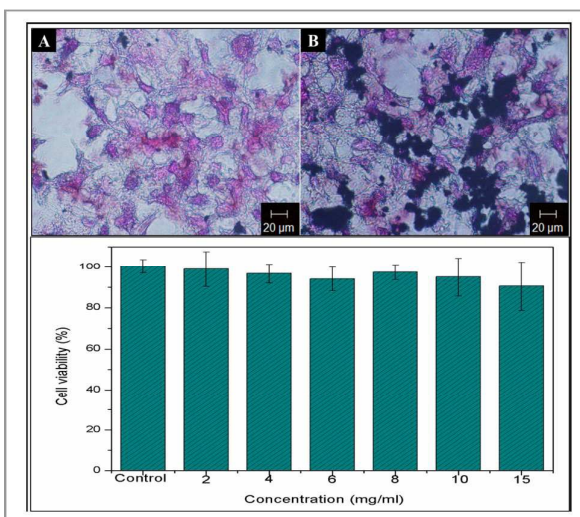


**Figure 4.** A&B) Intracellular localization of MSMFNPs by Prussian blue staining in 4T1 cell lines A) without & B) with an AMF for 5 min prior to incubation, C) In vitro biocompatibility of MSMFNPs at varying concentrations

The success of nanoparticle-assisted cancer diagnosis and treatment involves significant intracellular uptake of nanoparticles by tumor cells<sup>34</sup>. In light of previous studies depicting the enhanced cellular uptake of nanocomposites under a magnetic field,<sup>14, 35, 36</sup> we evaluated the intracellular localization of MSMFNPs in the presence and absence of an AMF for 5 min prior to the incubation of nanoparticles with 4T1 cell lines, followed by Prussian blue staining. After 2 hours of incubation, Prussian blue staining was carried out to analyze the intracellular uptake and distribution of MSMFNPs by 4T1 cell lines. As shown in Figure 4 A&B, most of the cells rendered blue colour, which was dispersed in the cytoplasm, indicating the successful internalization of MSMFNPs by 4T1 cells. Most importantly, the intensity in cells presented to the magnetic field (Figure 4 B) was much stronger than that in cells not presented to a magnetic field (Figure 4 A). This colour discrepancy revealed that the uptake efficiency was elevated explicitly in the presence of an external magnetic field due to the increased cell membrane permeability as a result of mild AMF heating indicating the enhanced internalization of nanoparticles for a short duration of time (2 h).<sup>35</sup> Biocompatibility must be analysed before a material can be used for any biological application.<sup>37, 38, 39</sup> Cell viability of MSMFNPs at various concentrations was tested against murine fibroblast (NIH3T3) cell lines after 1 day period using MTS assay. Cell viability results of the MSMFNPs were nearly equal to those of control cells at all concentrations (Figure 4C). This confirms the biocompatibility of the prepared MSMFNPs.

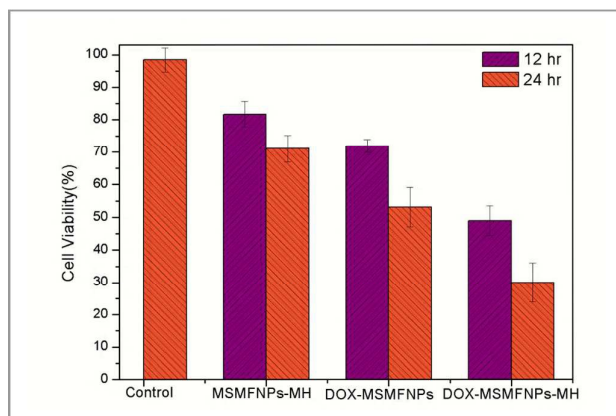


**Figure 5.** In-vitro anticancer effects of MSMFNPs on 4T1 cell lines

We investigated the possibility of employing MSMFNPs and DOX-MSMFNPs for the generation of localized tumoricidal effects in response to an AMF. The anticancer efficacies were tested on 4T1 cell lines in three scenarios, which include hyperthermia alone (MSMFNPs-MH), drug alone (DOX-MSMFNPs) and combined hyperthermia and chemotherapy (DOX-MSMFNPs-MH). Cell viabilities were tested at different incubation time after MH (Figure 5) using MTS assay. We found that average viabilities of treated cells decreased considerably after treatment. In the MSMFNPs-MH group, hyperthermia treatment caused the death of a considerable amount of cells (19%) 12 h after exposure to the AMF. Upon further incubation (to 24 h), cell viability decreased significantly (30%) without any treatment. This may be due to the inability of the injured cells survived suddenly after MH treatment to recover from the damage. The DOX-MSMFNP group also exhibited the same trend in viability with respect to incubation time (30% cell death after 12 h incubation, 47% cell death after 24 h incubation). This can be explained from the drug release profile (Figure 3B). MSMFNPs-DOX requires 12 h to release 80% of DOX. Therefore, the results are well-correlated with concentration-dependent drug cytotoxicity. In the DOX-MSMFNPs-MH group, the contribution from both DOX and hyperthermia play a crucial role in determining cell viability. Thus, as expected, DOX-MSMFNPs-MH exhibited increased cell cytotoxicity at 12 h (52%) and 24 h (71%) of incubation after MH treatment. The synergistic effect of the combined therapy can be explained by the physiological effect of mild hyperthermia on tumour vasculature, including increased blood flow, perfusion, and blood vessel pore size of the leaky tumour vasculature.<sup>40</sup> These factors facilitate DOX-MSMFNPs extravasation in tumour tissues, which precipitates enhanced drug accumulation along with effective hyperthermia. The results were validated qualitatively using a live/dead viability/cytotoxicity assay (Figure 6). The DOX-MSMFNPs-MH group with a 24-h incubation period exhibited intense red fluorescence (from dead cells) compared to the samples with a 12-h incubation period. This is in accordance with our in vitro cell viability results. These results confirm the enhanced antitumor efficacy of combined therapy in comparison with hyperthermia or chemotherapy alone. Thus,

the enhanced therapeutic efficacy of DOX-MSMFNPs-MH makes them a promising candidate for synergistic anticancer treatment.

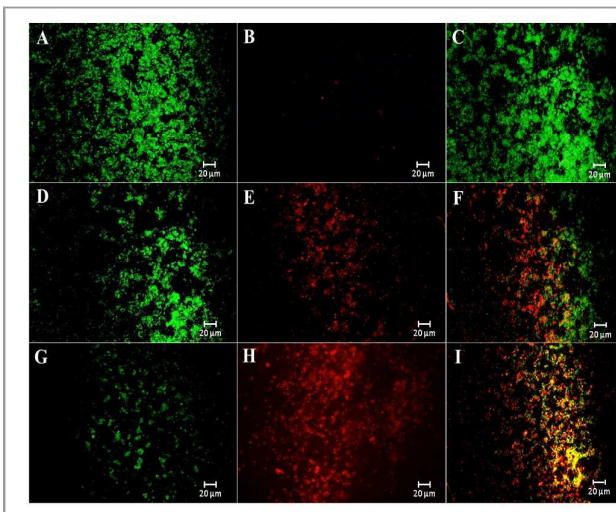


**Figure 6.** Live/dead assay displaying localized tumoricidal effects. A,B&C) MSMFNPs-MH, D,E&F) DOX-MSMFNPs-MH (12h post-MH treatment), and G,H&I) DOX-MSMFNPs-MH (24h post-MH treatment).

It has been reported that apoptosis is the primary cell death mechanism induced by mild hyperthermia and anticancer drugs.<sup>6, 22, 40</sup> Therefore, the apoptosis-inducing effect of DOX-MSMFNPs-MH was evaluated using the Magic Red caspase detection kit (Figure 7), which utilizes a red fluorogenic substrate for caspases 3 and 7. Both caspases 3 and 7 are essential proteases, playing central roles in triggering apoptotic processes in mammalian cells<sup>41</sup>. In the DOX-MSMFNPs-MH group, the cells exhibited strong red fluorescence in the cytoplasm, suggesting that DOX-MSMFNPs-MH significantly enhanced the activation of caspases in the cancer cells (Figure 7 C-F). The high intensity of red fluorescence in the Magic Red assay can be observed for DOX-MSMFNPs-MH after a 24 h incubation period. This can be directly correlated with apoptotic progression with time. As time passes, caspase activity increases due to increased apoptosis, resulting in increased red fluorescent signal. The results confirm that DOX-MSMFNPs-MH result in apoptosis-mediated tumoricidal effects.

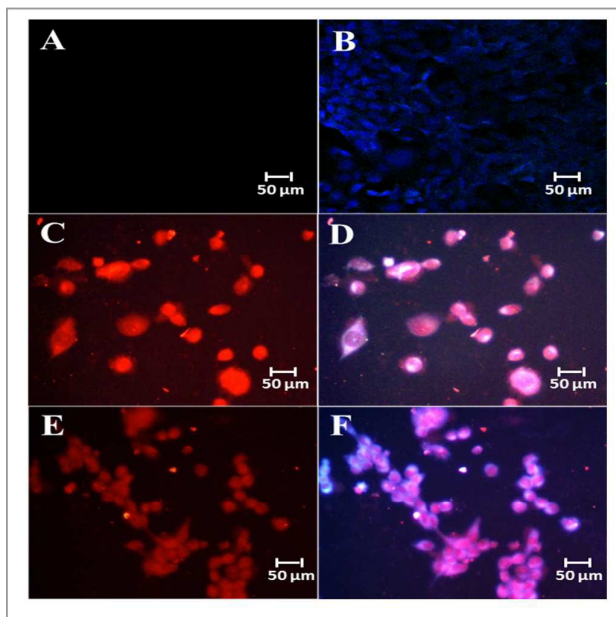


**Figure 7.** Magic Red TM assay showing the apoptosis-inducing effect (red fluorescence). A&B) MSMFNPs (control) C&D) DOX-MSMFNPs-MH (12 h post-MH treatment), and E&F) DOX-MSMFNPs-MH (24 h post-MH treatment). Cell nuclei were also stained with DAPI (blue fluorescence).

Further confirmation of the cell death mechanism was carried out by performing cytoskeletal F-actin staining using Phalloidin and Rhodamine B (Figure 8). The effect of DOX-MSMFNPs-MH on the F-actin organization in the 4T1 cells can be clearly visualized by the change in cell morphology. Typical features of apoptosis, such as membrane alteration and cytoskeletal damage including cell rounding and blebbing,<sup>42</sup> are clearly visualized in both stains in the DOX-MSMFNPs-MH group compared to the control. After 12 h of incubation post-MH, cytoskeletons were abridged and cells shrank (Figure 8B&E). Many of the cells exhibited shrunken morphology with membrane blebbing, which completely disappeared after 24 h (Figure 8C&F). In short, after 24 h of incubation, the cytoskeletons were seriously damaged as observed in both Phalloidin and Rhodamine B staining (Figure 8C&F). Cleavage and disruption of the actin cytoskeleton was observed in many cases of apoptosis.<sup>43, 22, 44</sup> The steady decline in viability of the cytoskeletal morphology of the DOX-MSMFNPs-MH treated cells clearly indicates that the treated cells are prone to perturbation and thereby initiation of apoptotic signals. Therefore we can conclude that the cytoskeletal damage caused by the DOX-MSMFNPs-MH is irreversible, and the cells cannot recover their original structure.

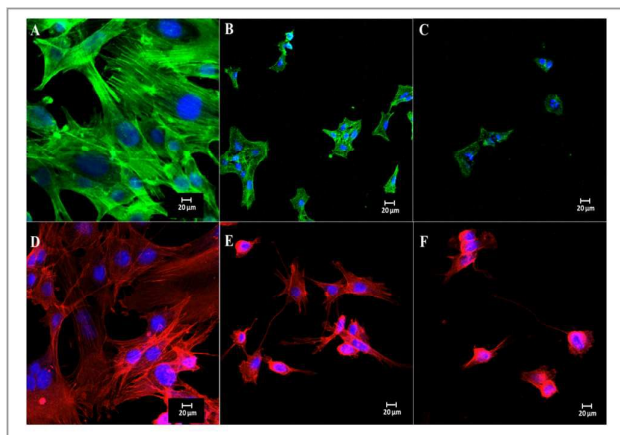


**Figure 8.** In vitro cytoskeletal imaging with A-C) Alexa Fluor® 488 Phalloidin (green fluorescence). A) MSMFNPs (control), B&C) DOX-MSMFNPs-MH (12 h and 24 h post-MH treatment), and D-F) Rhodamine Phalloidin (red fluorescence), D) MSMFNPs (control), E&F) DOX-MSMFNPs-MH (12 h and 24 h post- MH treatment). Cell nuclei were also stained with DAPI (blue fluorescence).

#### 4. Conclusions

In conclusion, we developed novel, superparamagnetic core-shell MFNP-encapsulated mesoporous silica nanoparticles (MSMFNPs) loaded with DOX for the combined application of hyperthermia and chemotherapy. The DOX-loaded MSMFNPs delivered superior heating ability, along with tumor-specific cationic DOX release, resulting in a synergistic anticancer effect. Furthermore, DOX-MSMFNPs-MH effectively eradicated target cancer cells through apoptosis-mediated tumoricidal effects. The steady attenuation in the viability of the cytoskeletal morphology of the DOX-MSMFNPs-MH treated cells resulted in irreversible cytoskeletal damage after a 24-h incubation period, demonstrating its efficacy as a novel nanotherapeutic agent for cancer therapy.

#### Acknowledgements

This research was supported by grants from the Basic Science Research Program through the National Research Foundation of Korea (NRF), funded by the Ministry of Education, Science and Technology (Project no. 2013-012911 and 2013R1A2A2A04015484).

#### Notes and references

\*Corresponding authors

[chskim@jbnu.ac.kr](mailto:chskim@jbnu.ac.kr)

[biochan@jbnu.ac.kr](mailto:biochan@jbnu.ac.kr)

[afeesh@jbnu.ac.kr](mailto:afeesh@jbnu.ac.kr), [afeeshnano@gmail.com](mailto:afeeshnano@gmail.com)

† Electronic Supplementary Information (ESI) available (Magnetic property measurements, AMF-Induced Heat Generation Properties and calculation of SAR, Field-dependent magnetization of MFNPs and MSMFNPs, AMF-induced heating ability of MSMFNPs at varying concentrations, live/dead analysis data)

Journal Name

- R. Hao, R. J. Xing, Z. C. Xu, Y. L. Hou, S. Gao and S. H. Sun, *Adv Mater*, 2010, **22**, 2729-2742.
- A. R. K. Sasikala, A. GhavamiNejad, A. R. Unnithan, R. G. Thomas, M. Moon, Y. Y. Jeong, C. H. Park and C. S. Kim, *Nanoscale*, 2015, **7**, 18119-18128.
- A. R. U. Arathyram Ramachandra Kurup Sasikala, Yeo-Heung Yun, Chan Hee Park, Cheol Sang Kim, *Acta Biomater*, 2015, DOI: doi:10.1016/j.actbio.2015.12.015.
- D. F. Liu, W. Wu, J. J. Ling, S. Wen, N. Gu and X. Z. Zhang, *Adv Funct Mater*, 2011, **21**, 1498-1504.
- C. B. Huang, S. J. Soenen, J. Rejman, J. Trekker, C. X. Liu, L. Lagae, W. Ceelen, C. Wilhelm, J. Demeester and S. C. De Smedt, *Adv Funct Mater*, 2012, **22**, 2479-2486.
- Y. J. Kim, M. Ebara and T. Aoyagi, *Adv Funct Mater*, 2013, **23**, 5753-5761.
- J. R. McCarthy and R. Weissleder, *Adv Drug Deliver Rev*, 2008, **60**, 1241-1251.
- K. C. Barick, S. Singh, N. V. Jadhav, D. Bahadur, B. N. Pandey and P. A. Hassan, *Adv Funct Mater*, 2012, **22**, 4975-4984.
- I. Koh and L. Josephson, *Sensors-Basel*, 2009, **9**, 8130-8145.
- J. H. Gao, H. W. Gu and B. Xu, *Accounts Chem Res*, 2009, **42**, 1097-1107.
- A. H. Lu, E. L. Salabas and F. Schuth, *Angew Chem Int Edit*, 2007, **46**, 1222-1244.
- C. Argyo, V. Weiss, C. Brauchle and T. Bein, *Chem Mater*, 2014, **26**, 435-451.
- S. Laurent, D. Forge, M. Port, A. Roch, C. Robic, L. V. Elst and R. N. Muller, *Chem Rev*, 2008, **108**, 2064-2110.
- Y. Qu, J. B. Li, J. Ren, J. Z. Leng, C. Lin and D. L. Shi, *Nanoscale*, 2014, **6**, 12408-12413.
- Z. S. Liang, X. G. Li, Y. G. Xie and S. Y. Liu, *Biomed Mater*, 2014, **9**.
- T. M. Sun, Y. S. Zhang, B. Pang, D. C. Hyun, M. X. Yang and Y. N. Xia, *Angew Chem Int Edit*, 2014, **53**, 12320-12364.
- M. Colilla, B. Gonzalez and M. Vallet-Regi, *Biomater Sci-Uk*, 2013, **1**, 114-134.
- N. Z. Knezevic, E. Ruiz-Hernandez, W. E. Hennink and M. Vallet-Regi, *Rsc Adv*, 2013, **3**, 9584-9593.
- D. Yoo, J. H. Lee, T. H. Shin and J. Cheon, *Accounts Chem Res*, 2012, **45**, 1622-1622.
- P. Pradhan, J. Giri, R. Banerjee, J. Bellare and D. Bahadur, *J Magn Magn Mater*, 2007, **311**, 208-215.
- E. Peng, J. Ding and J. M. Xue, *New J Chem*, 2014, **38**, 2312-2319.
- N. K. Prasad, K. Rathinasamy, D. Panda and D. Bahadur, *J Mater Chem*, 2007, **17**, 5042-5051.
- M. R. Barati, K. Suzuki, C. Selomulya and J. S. Garitaonandia, *Ieee T Magn*, 2013, **49**, 3460-3463.
- X. F. Zhang, S. Mansouri, L. Clime, H. Q. Ly, L. H. Yahia and T. Veres, *J Mater Chem*, 2012, **22**, 14450-14457.
- M. Simeonova, G. Ivanova, V. Enchev, N. Markova, M. Kamburov, C. Petkov, A. Devery, R. O'Connor and D. Brougham, *Acta Biomater*, 2009, **5**, 2109-2121.
- P. Drake, H. J. Cho, P. S. Shih, C. H. Kao, K. F. Lee, C. H. Kuo, X. Z. Lin and Y. J. Lin, *J Mater Chem*, 2007, **17**, 4914-4918.
- R. Ghosh, L. Pradhan, Y. P. Devi, S. S. Meena, R. Tewari, A. Kumar, S. Sharma, N. S. Gajbhiye, R. K. Vatsa, B. N. Pandey and R. S. Ningthoujam, *J Mater Chem*, 2011, **21**, 13388-13398.

28. X. F. Zhang, L. Clime, H. Roberge, F. Normandin, L. Yahia, E. Sacher and T. Veres, *J Phys Chem C*, 2011, **115**, 1436-1443.
29. N. Andhariya, B. Chudasama, R. V. Mehta and R. V. Upadhyay, *J Nanopart Res*, 2011, **13**, 1677-1688.
30. Q. L. Li, W. X. Gu, H. Gao and Y. W. Yang, *Chem Commun*, 2014, **50**, 13201-13215.
31. Y. A. Ma, H. Gao, W. X. Gu, Y. W. Yang, Y. N. Wang, Y. G. Fan, G. L. Wu and J. B. Ma, *Eur J Pharm Sci*, 2012, **45**, 65-72.
32. J. Kim, H. S. Kim, N. Lee, T. Kim, H. Kim, T. Yu, I. C. Song, W. K. Moon and T. Hyeon, *Angew Chem Int Edit*, 2008, **47**, 8438-8441.
33. C. L. Tao and Y. F. Zhu, *Dalton T*, 2014, **43**, 15482-15490.
34. X. S. Liu, Y. J. Chen, H. Li, N. Huang, Q. Jin, K. F. Ren and J. Ji, *Acs Nano*, 2013, **7**, 6244-6257.
35. C. Wang, H. Xu, C. Liang, Y. M. Liu, Z. W. Li, G. B. Yang, H. Cheng, Y. G. Li and Z. Liu, *Acs Nano*, 2013, **7**, 6782-6795.
36. Q. Liu, J. X. Zhang, W. L. Xia and H. C. Gu, *Nanoscale*, 2012, **4**, 3415-3421.
37. A. Gautam and F. C. J. M. van Veggel, *J Mater Chem B*, 2013, **1**, 5186-5200.
38. A. R. Unnithan, A. R. K. Sasikala, Y. Sathishkumar, Y. S. Lee, C. H. Park and C. S. Kim, *Ceram Int*, 2014, **40**, 12003-12012.
39. A. R. Unnithan, A. R. K. Sasikala, P. Murugesan, M. Gurusamy, D. M. Wu, C. H. Park and C. S. Kim, *Int J Biol Macromol*, 2015, **77**, 1-8.
40. A. Hervault and N. T. K. Thanh, *Nanoscale*, 2014, **6**, 11553-11573.
41. W. C. Earnshaw, L. M. Martins and S. H. Kaufmann, *Annu Rev Biochem*, 1999, **68**, 383-424.
42. R. C. Taylor, S. P. Cullen and S. J. Martin, *Nat Rev Mol Cell Bio*, 2008, **9**, 231-241.
43. F. Luchetti, F. Mannello, B. Canonico, M. Battistelli, S. Burattini, E. Falcieri and S. Papa, *Apoptosis*, 2004, **9**, 635-648.
44. T. Mashima, M. Naito, K. Noguchi, D. K. Miller, D. W. Nicholson and T. Tsuruo, *Oncogene*, 1997, **14**, 1007-1012.

Schematic illustration of the synergistic anticancer mechanism exhibited by Smart Mesoporous Silica Nanoparticles by combining the Cationic Doxorubicin Delivery with Hyperthermia

